Supporting Information

Molybdenum-Iron-Cobalt Oxyhydroxide with Rich Oxygen Vacancies for Oxygen Evolution Reaction

Yechuan Zhang,[ab, ‡] *Zhengxiang Gu,*[a, ‡] *Jingxiu Bi,*[b] *Yan Jiao*[b,*]

Y. Zhang, Dr. Z. Gu,

Huaxi MR Research Center (HMRRC), Department of Radiology, State Key Laboratory of Biotherapy, West China Hospital, Sichuan University, Chengdu 610041, China.

E-mail: zxgu16@scu.edu.cn

Y. Zhang, A/Prof. Jingxiu Bi, A/Prof. Y. Jiao,

School of Chemical Engineering and Advanced Materials, University of Adelaide, SA 5005, Australia.

*E-mail: yan.jiao@adelaide.edu.au

‡Y. Z. and Z.G. contributed equally to this work.

*Corresponding author.

Experimental Section

All materials were of analytical grade and used without further purification.

Synthesis of $MoO_xCo(OH)_{2-x}$

In a typical synthesis, 2 mmol of $Na_2MoO_4 \cdot 2H_2O$ and 4 mmol of glucose were dissolved into 50 mL of DI water. The mixture was treated with an intense ultrasonication for a few minutes and then transferred to a 1000 mL Teflon stainless steel autoclave. Afterwards, $Co(OH)_2$ nanowires supported was immersed in the reaction solution. The autoclave was sealed and maintained at 150 °C for 6 h and then cooled to room temperature.

Structure Characterizations

A field emission scanning electron microscopy (FESEM; ZEISS-Merlin), a transmission electron microscopy (TEM, JEOL-2010) with energy dispersive X-ray spectroscopy (EDX), and a high-resolution TEM (HRTEM, JEOL-2010) were used to characterize the morphology and composition of samples. (XRD) curves of samples were recorded on Rigaku at 40 kV and 40 mA, and X-ray photoelectron spectroscopy (XPS) curves are obtained on a PHI Quantera SXM (ULVAC-PHI) instrument to determine the compositions and the valence states of the elements in the samples.

Electrochemical measurements.

All electrochemical measurements were performed on a CHI 760E electrochemical work station with a typical three-electrode setting at room temperature. A graphite rod and a Hg/HgO electrode were selected as a counter and reference electrode, respectively. The self-supporting array grown on carbon cloth (1×1 cm, mass loading ~ 2.5 mg/cm^{-2}) was directly used as a working electrode. The electrochemical data were collected in an electrolyte of 1.0 M KOH. The measured potentials via the Hg/HgO electrode were converted to those based on a reversible hydrogen electrode (RHE) by the Nernst equation: E(RHE) = E(Hg/HgO) + 0.0591*pH + 0.098. The overpotential (η) was calculated according to the following equation: η = E(RHE)-1.23 V. Linear sweep voltammetry curves for OER were established at a scanning rate of 5 mV/s before 50 cycles of the cyclic voltammetry tests at a scan rate

of 50 mV/s were conducted to obtain stable curves. The Tafel slopes were obtained from the polarization curves by the equation, $\eta = a + b \log (i)$. The chronoamperometry was operated to evaluate the stability under different current densities. Electrochemical impedance spectroscopy (EIS) measurements were performed over a frequency range of $0.1\text{-}10^6$ Hz by applying an AC amplitude of 50 mV. All data presented were within 90% iR-correction.

Figures

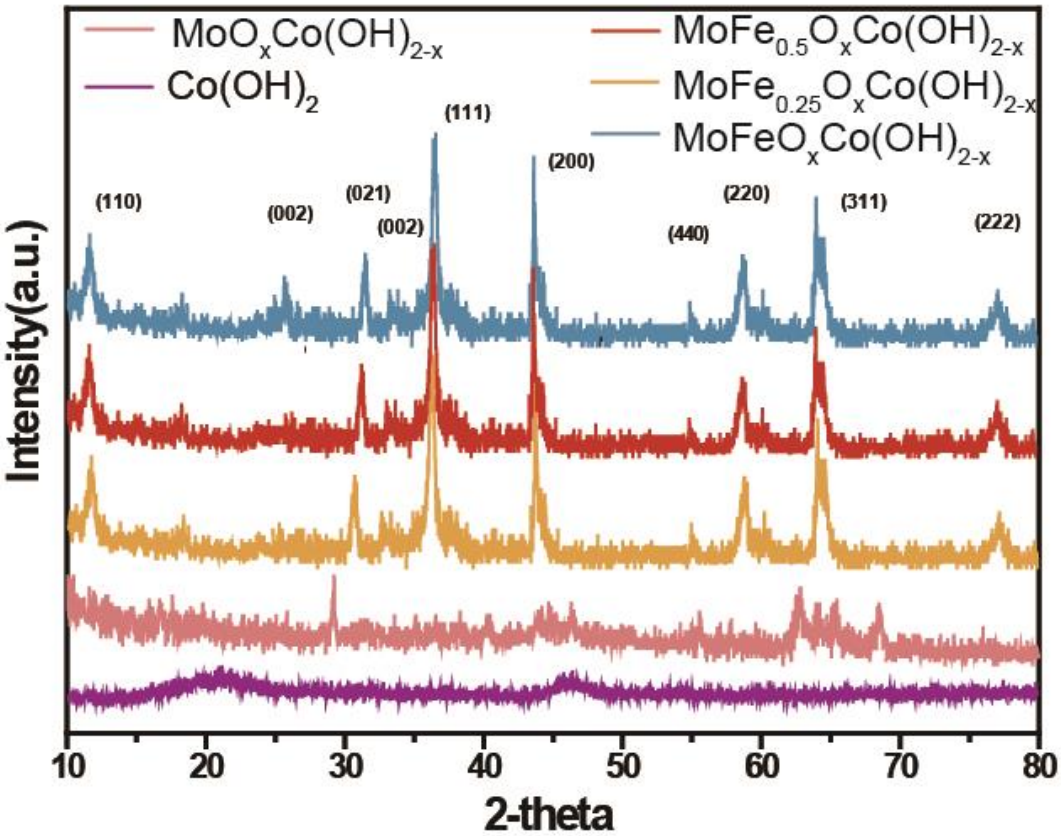

Figure S1. (a) XRD patterns of different electrocatalysts.

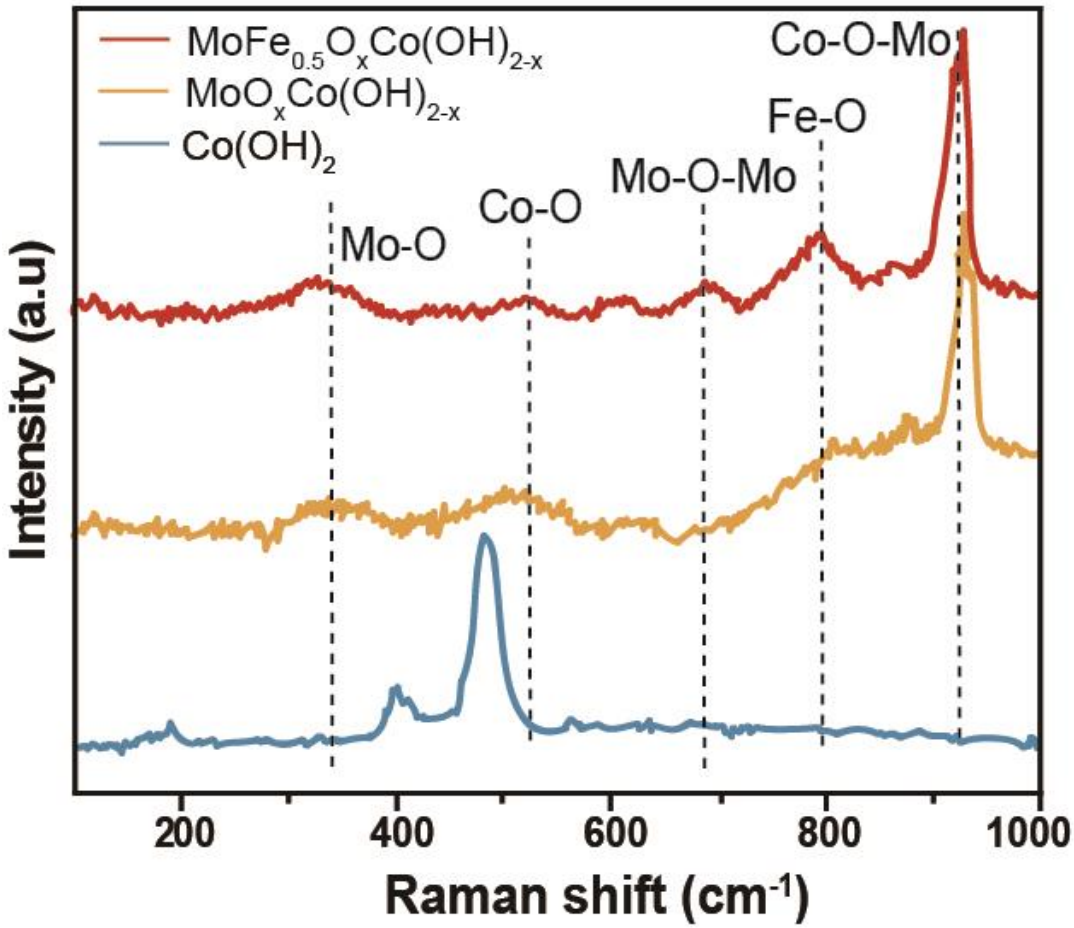

Figure S2. (a) Raman spectra of $MoO_xCo(OH)_{2-x}$, $MoFe_{0.5}O_xCo(OH)_{2-x}$, and $Co(OH)_2$ electrocatalysts.

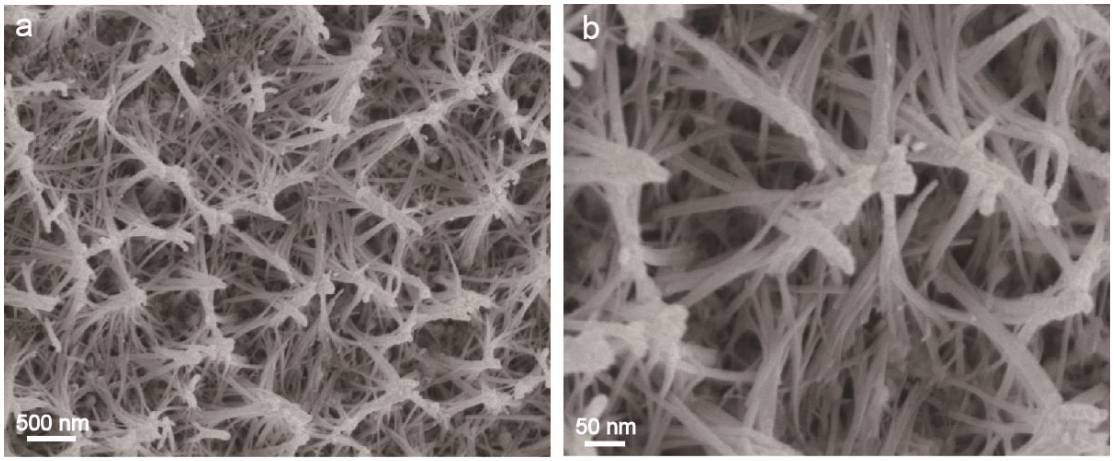

Figure S3. (a, b) SEM images of $Co(OH)_2$.

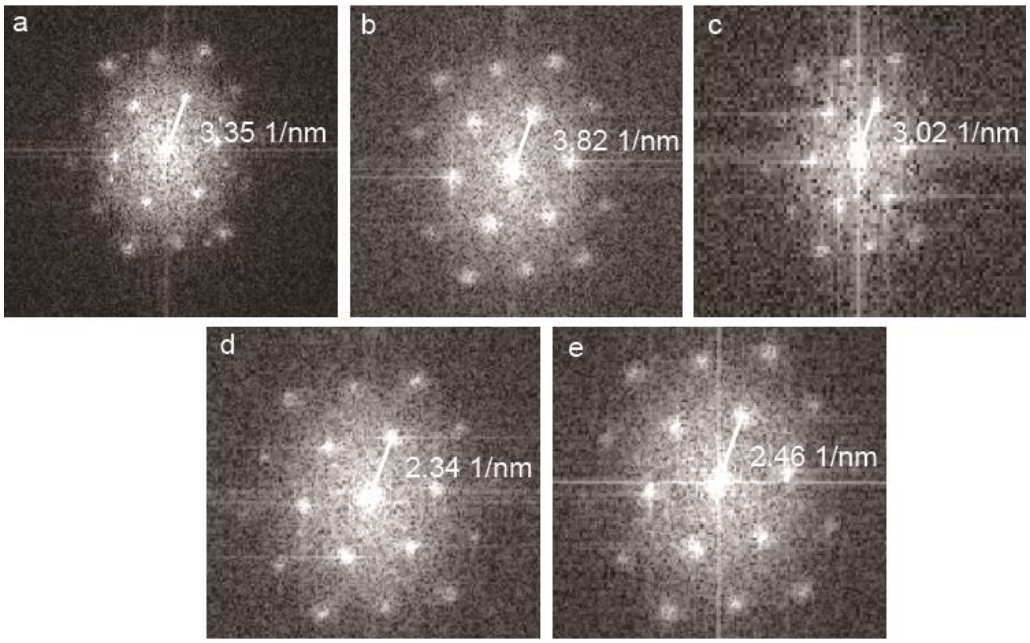

Figure S4. Images of Fourier transform corresponding to Fig 2a and 2c that reveal the lattice spacing of $MoFe_{0.5}O_xCo(OH)_{2-x}$.

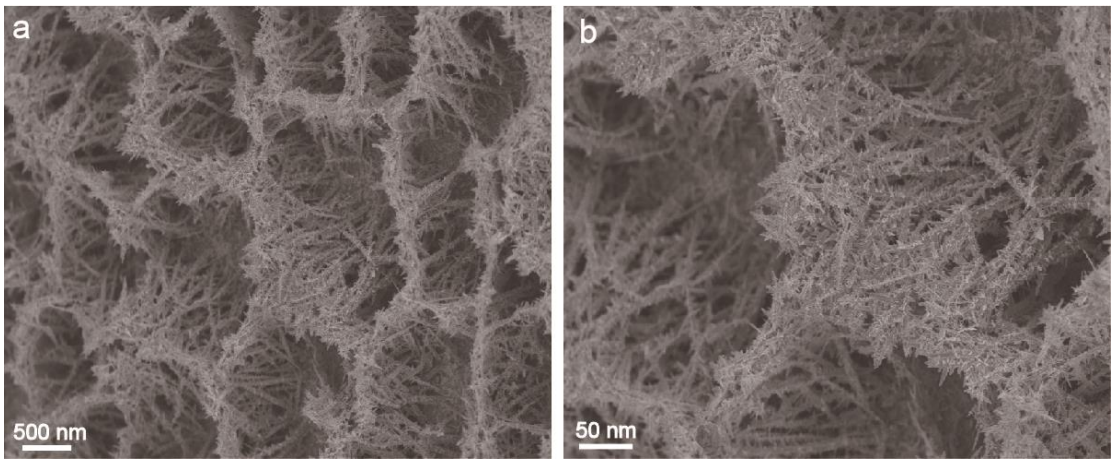

Figure S5. (a, b) SEM images of $MoFe_{0.5}O_xCo(OH)_{2-x}$.

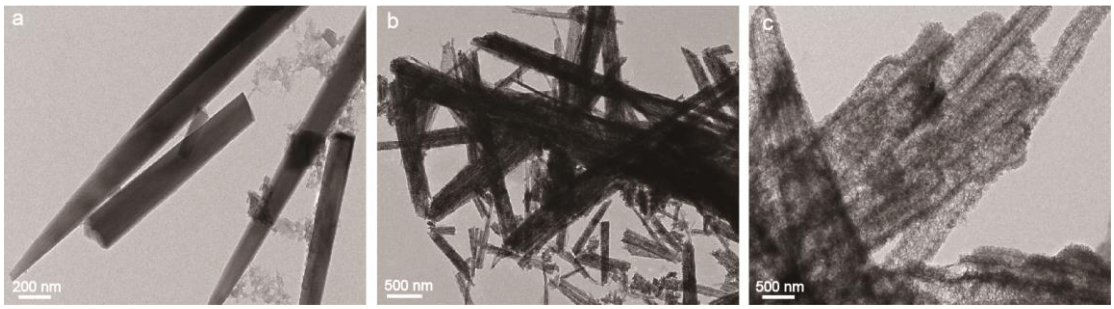

Figure S6. TEM images of (a)$Co(OH)_2$, (b) $MoFeO_xCo(OH)_{2-x}$, (c) $MoFe_{0.5}O_xCo(OH)_{2-x}$.

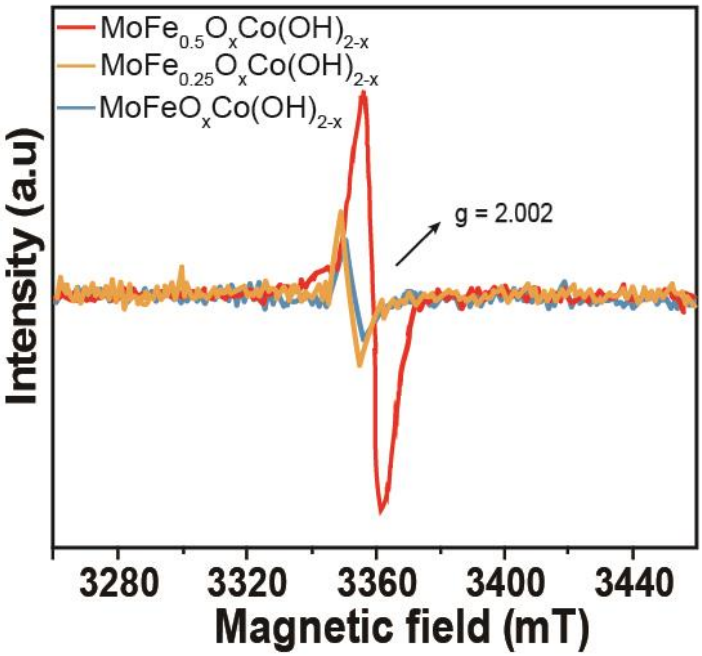

Figure S7. EPR spectra of $MoFeO_xCo(OH)_{2-x}$, $MoFe_{0.25}O_xCo(OH)_{2-x}$, and $MoFe_{0.5}O_xCo(OH)_{2-x}$.

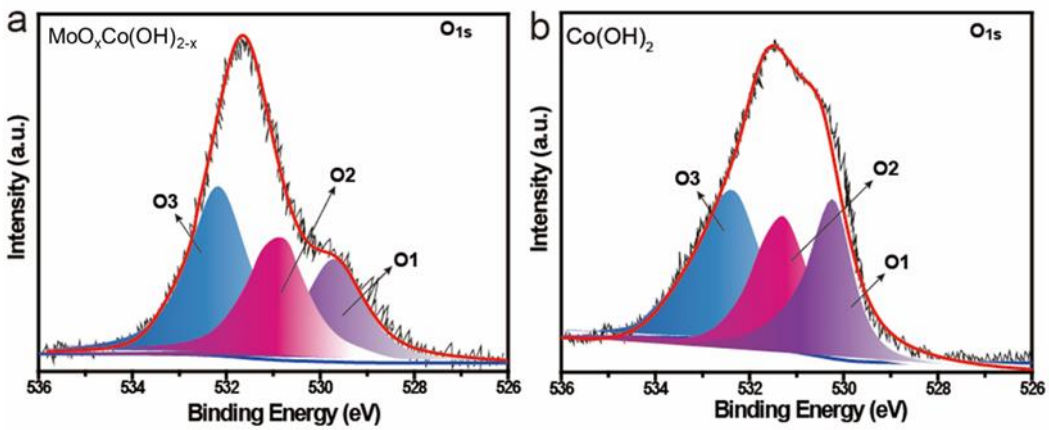

Figure S8. O1s XPS of comparative (a) $MoO_xCo(OH)_{2-x}$ and (b) $Co(OH)_2$.

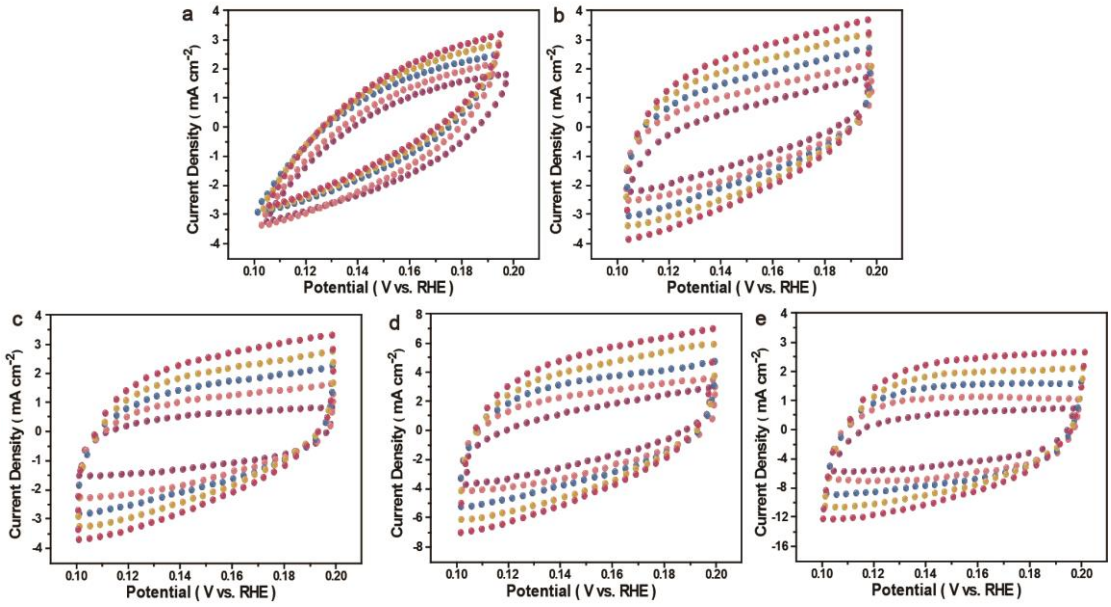

Figure S9. (a) CV curves of (a) $Co(OH)_2$, (b) $MoO_xCo(OH)_{2-x}$, (c) $MoFe_{0.25}O_xCo(OH)_{2-x}$, (d) $MoFe_{0.5}O_xCo(OH)_{2-x}$, (e) $MoFeO_xCo(OH)_{2-x}$ electrocatalysts at scan rates from 10 to 50 mV s^{-1}.

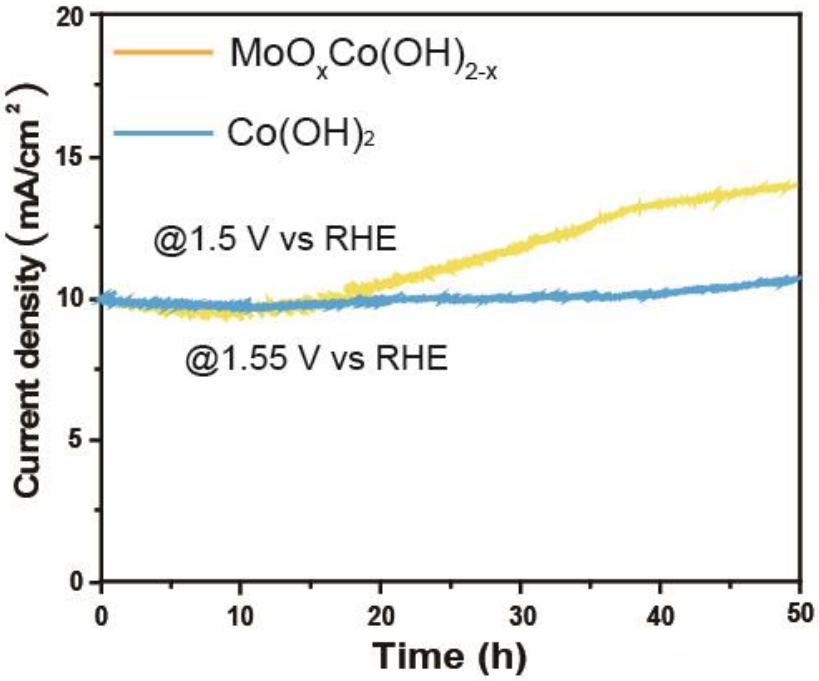

Figure S10. Long-term durability test of $Co(OH)_2$ and $MoO_xCo(OH)_{2-x}$ at different potentials for OER.

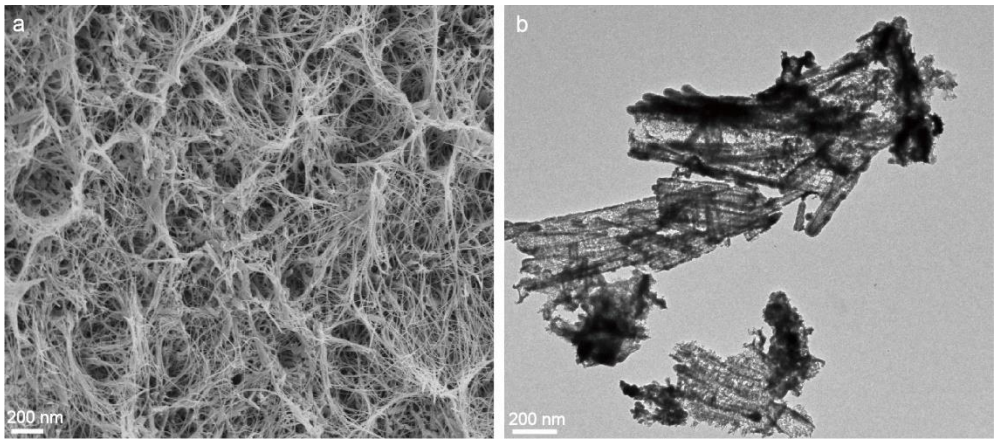

Figure S11. (a) SEM image and (b) TEM image of $MoFe_{0.5}O_xCo(OH)_{2-x}$ after the stability test.

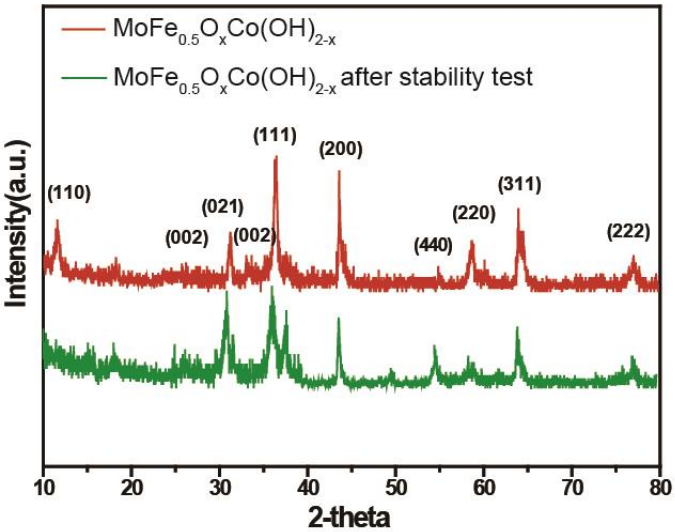

Figure S12. XRD pattern of $MoFe_{0.5}O_xCo(OH)_{2-x}$ before and after the stability test.

Table S1. The metallic composition of $MoO_xCo(OH)_{2-x}$, $MoFe_{0.5}O_xCo(OH)_{2-x}$, $MoFe_{0.25}O_xCo(OH)_{2-x}$, and $MoFeO_xCo(OH)_{2-x}$, catalyst by ICP-MS. Regardless of oxygen in this characterization.

Sample	Co (at.%)	Mo (at.%)	Fe (at.%)
$MoO_xCo(OH)_{2-x}$	90.13	9.87	-
$MoFe_{0.25}O_xCo(OH)_{2-x}$	88.46	9.01	2.53
$MoFe_{0.5}O_xCo(OH)_{2-x}$	86.97	7.51	5.52
$MoFeO_xCo(OH)_{2-x}$	83.61	6.21	10.18

Table S2. Comparison of the OER activities of the $MoFe_{0.5}O_xCo(OH)_{2-x}$ sample in this work with recently-reported catalysts.

catalysts	Overpotential (mV)	j /(mA cm^{-2})	Tafel slope (mV dec^{-1})	Reference
$MoFe_{0.5}O_xCo(OH)_{2-x}$	**223**	**10**	**43.6**	**This work**
CoFeV-LDH	242	10	57	S1
CoMoV-LDH	270	10	106	S2
CoMo hydr(oxy)oxide	377	10	41.88	S3
CoFe-LDH	320	10	53	S4
$Fe_xCo_{1-x}OOH$	266	10	30.0	S5
Ir-doped $NiV(OH)_2$	260	10	55.3	S6
$NiCo_{16-x}P_6$	290	10	66	S7
CoP-CeO_2	224	10	90.3	S8
Pt-Cu@Cu_xO	250	10	56	S9
NiCoMo	304	10	56.4	S10

References：

S1. Y. M. Hu, Z. L. Wang, W. J. Liu, L. Xu, M. L. Guan, Y. P. Huang, Y. Zhao, J. Bao and H. M. Li, *Acs Sustain Chem Eng*, 2019, **7**, 16828-16834.

S2. J. Bao, Z. L. Wang, J. F. Xie, L. Xu, F. C. Lei, M. L. Guan, Y. Zhao, Y. P. Huang and H. M. Li, *Chem Commun*, 2019, **55**, 3521-3524.

S3. S. Bera, W. J. Lee, E. K. Koh, C. M. Kim, S. Ghosh, Y. Yang and S. H. Kwon, *J Phys Chem C*, 2020, **124**, 16879-16887.

S4. Q. Zhou, Y. P. Chen, G. Q. Zhao, Y. Lin, Z. W. Yu, X. Xu, X. L. Wang, H. K. Liu, W. P. Sun and S. X. Dou, *Acs Catal*, 2018, **8**, 5382.

S5. S. H. Ye, Z. X. Shi, J. X. Feng, Y. X. Tong and G. R. Li, *Angew Chem Int Edit*, 2018, **57**, 2672-2676.

S6. S. Li, C. Xi, Y. Z. Jin, D. Y. Wu, J. Q. Wang, T. Liu, H. B. Wang, C. K. Dong, H. Liu, S. A. Kulinich and X. W. Du, *Acs Energy Lett*, 2019, **4**, 1823-1829.

S7. Y. F. Zhao, J. Q. Zhang, Y. H. Xie, B. Sun, J. J. Jiang, W. J. Jiang, S. B. Xi, H. Y. Yang, K. Yan, S. J. Wang, X. Guo, P. Li, Z. J. Han, X. Y. Lu, H. Liu and G. X. Wang, *Nano Lett*, 2021, **21**, 823-832.

S8. M. Li, X. C. Pan, M. Q. Jiang, Y. F. Zhang, Y. W. Tang and G. T. Fu, *Chem Eng J*, 2020, **395**.

S9. D. T. Tran, H. T. Le, T. L. L. Doan, N. H. Kim and J. H. Lee, *Nano Energy*, 2019, **59**, 216-228.

S10. S. Y. Hao, L. C. Chen, C. L. Yu, B. Yang, Z. J. Li, Y. Hou, L. C. Lei and X. W. Zhang, *Acs Energy Lett*, 2019, **4**, 952-959.